The fracture toughness of octet-truss lattices

M.R. O'Masta [a, *], L. Dong [b], L. St-Pierre [a], H.N.G. Wadley [b] and V.S. Deshpande [a]

[a] *Engineering Department, University of Cambridge, Trumpington Street, Cambridge CB2 1PZ, UK*

[b] *Department of Material Science & Engineering, School of Engineering and Applied Science, University of Virginia, Charlottesville, VA 22904, USA*

Abstract

The only engineering materials with both high strength and toughness, and with densities less than 1000 kg m^{-3}, are natural materials (woods) and some plastics. Cellular structures such as the octet lattice, when made from periodic arrangements of strong, low-density metallic trusses, are known to have high specific strengths and elastic moduli. However, much less is known of their resistance to fracture. Here we investigate the fracture toughness of a Ti-6Al-4V alloy octet-lattice truss structure manufactured using a 'snap-fit' method. The samples had densities between 360 and 855 kg m^{-3} (relative densities of 8-19%) and free truss lengths between 4 and 15 mm. Their fracture resistance was determined using the *J*-integral compliance method applied to single-edge notched bend specimens. The toughness is shown to increase linearly with the relative density and with the square root of the cell size, while the strength was confirmed to scale only with relative density and the strength of the solid. A moderate increase in resistance with crack length (an R-curve effect) was seen for the higher relative density and larger cell size samples. With a fracture toughness between 2 and 14 MPa m$^{1/2}$ and a compressive strength between 20 and 70 MPa, these structures offer a new lightweight engineering material solution for use at temperatures up to 450C.

* Corresponding author; M.R. O'Masta; E-mail address: mro27@cam.ac.uk

1. Introduction

Materials for load bearing applications must usually be stiff, strong and tough, and for many applications, they must also be lightweight. While many metallic alloys offer combinations of high yield strength (σ^y = 100 to 2000 MPa) and fracture toughness (K_{Ic} = 10 to 500 MPa m$^{1/2}$), apart from those based upon (toxic) beryllium and (corrosion susceptible) magnesium alloys, their densities are all well above 2000 kg m^{-3}, Fig. 1. Below 1000 kg m^{-3}, various cellular materials made from metals, polymers and natural materials abound, but wood offers the best combination of structural properties if loads are applied parallel to the direction of the grain. However, it suffers from significant anisotropy, and is more problematic to use in multi-axially loading scenarios where fracture can occur in the longitudinal grain direction. A method to design high specific (density scaled) mechanical properties is through the strategic arrangement of trusses in a periodic array, thus creating a cellular material (Gibson and Ashby, 1997; Wadley, 2006; Kooistra et al., 2004; Ashby, 2011). Structures comprised of stretching dominated unit cells, such as the (2D) triangular or (3D) octet truss, Fig. 2a and b, are stiffer and stronger than their (low node connectivity) bending dominated counterparts (Deshpande et al., 2001a). Furthermore, these two unit cells are nearly isotropic (Deshpande et al., 2001b), and recent studies by Dong et al. (Dong et al., 2015) have shown that lightweight octet lattices made from titanium alloys can reach compressive strengths of 60 MPa at densities of 720 kg m^{-3}. However, there is a paucity of data on the fracture toughness of 3D lattice materials.
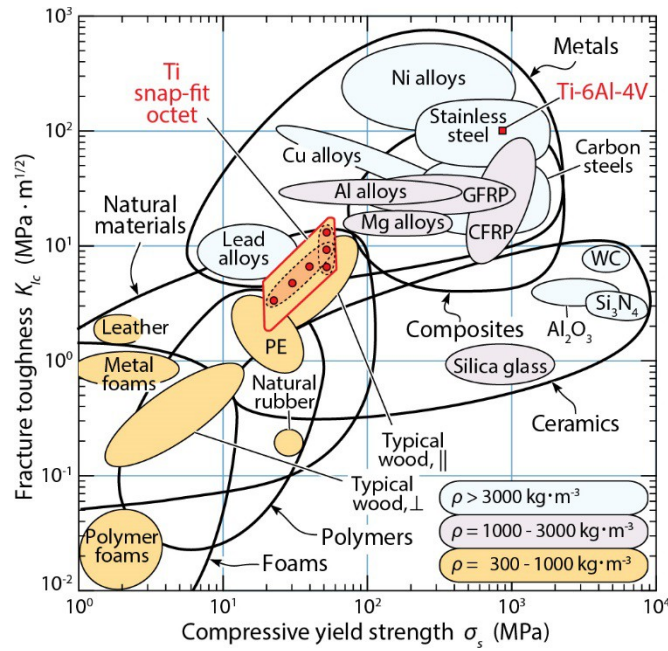
Figure 1. Material property map of the fracture toughness, K_{Ic}, and compressive yield strength, σ^y, space. Snap-fit octet truss data collected in present study are plotted with red circles. Material values were sourced from Ref. (*CES EduPack*, 2015). Abbreviations are as follows: PE, polyethylene; CFRP, carbon fiber reinforced plastic; GFRP, glass fiber reinforced plastic.
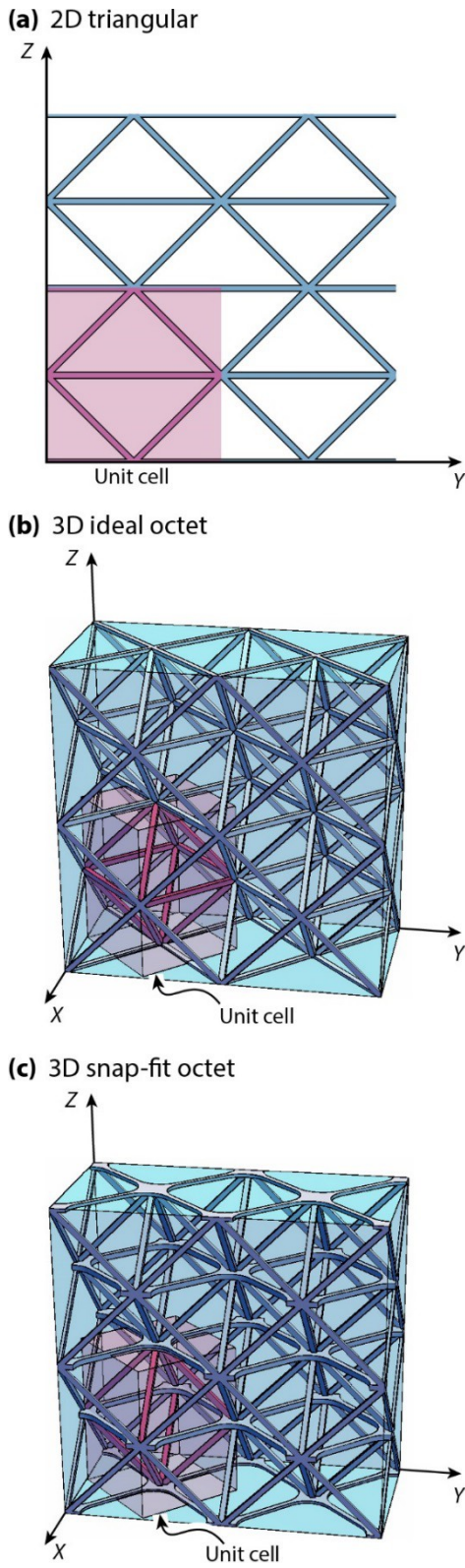
Figure 2. Schematic illustrations of (a) a 2D triangular lattice, (b) a 3D octet lattice and (c) a 3D 'snap-fit' fabricated octet lattice.

The octet truss lattice comprises a 3D arrangement of tetrahedral sub lattices, where the nodes form a face centered cubic structure, Fig. 2b. Fabrication of millimeter scale octet truss lattices has been accomplished using a snap-fit method (Dong et al., 2015; Dong and Wadley, 2015; Finnegan et al., 2007), a reverse assembly technique(Cheung and Gershenfeld, 2013), and an investment casting approach (Deshpande et al., 2001b). Sub-millimeter structures have begun to be made using stereo-lithography combined with electrolysis nickel plating or vapor deposition (Bauer et al., 2014; Torrents et al., 2012; Zheng et al., 2014), by combined techniques which involve two photon lithography (TLP), direct laser writing (DLW), atomic layer deposition (ALD), and O_2 plasma etching (Jang et al., 2013; Meza et al., 2014). Fabrication of nanoscale lattices (metamaterials) has also begun to be investigated using direct write methods (Bauer et al., 2016; Greer, 2015; Montemayor et al., 2015).

The scaling relationships between lattice geometry and lattice relative density, $\acute{\rho}$, Young's modulus, E, and compressive strength, σ^p, for an ideal octet cellular structure are summarized in Table 1. The relative density, $\acute{\rho}$, scales with the ratio of the (square cross-sectioned) truss thickness, t, to the truss length, l. Both E and σ^p, scale linearly with $\acute{\rho}$ and the parent material properties (viz. the Young's modulus, E_s, and yield strength, σ_s, respectively), which is characteristic of stretching dominated structures. The snap-fit structure studied by Dong et al. (Dong et al., 2015), Fig 2c, shows similar scaling of $\acute{\rho}$, E and σ^p, to an ideal octet truss, after accounting for extra nodal volume needed to implement this assembly route, Table 1. The

variables *b, c, h, h_{tab},* and *l* in Table 1 are defined in Fig. 3, where *l* is the free truss length between the nodes.

Table 1. Material property scaling for three cellular materials

	Triangular	Ideal octet	Snap-fit octet
$\dot\rho$	$2\sqrt{3}\dfrac{t}{l}$ [a]	$6\sqrt{2}\left(\dfrac{t}{l}\right)^2$ [b]	$6\sqrt{2}\left(\dfrac{t}{l}\right)^2 \dfrac{(1+\acute{K}_5)}{(1+\acute{K}_3)(1+\acute{K}_4)^2}$ [c]
E_{XX}/E_s	$\dfrac{1}{3}\dot\rho$ [a]	$\dfrac{1}{9}\dot\rho$ [b]	$\dfrac{1}{9}\dot\rho\dfrac{(1+\acute{K}_4)^2}{(1+\acute{K}_5)}$ [d]
σ_{XX}^p/σ_s	$\dfrac{1}{3}\dot\rho$ [a]	$\dfrac{1}{3}\dot\rho$ [b]	$\dfrac{1}{3}\dot\rho\dfrac{(1+\acute{K}_4)}{(1+\acute{K}_5)}$ [d]
$K_{Ic}/(\sigma_s\sqrt{l})$	$\sim\dfrac{1}{2}\dot\rho$ [e]	N/A	$0.45\,\dot\rho\sqrt{\dfrac{(1+\acute{K}_3)^2+(1+\acute{K}_4)^2}{2}}$ [present study]

Constants: $\acute{K}_3=\sqrt{2}(h+2h_{tab})/l$, $\acute{K}_4=(b+c)/(\sqrt{2}l)$ and $\acute{K}_5=4.185(t/l)$. References: [a] (Gibson and Ashby, 1997); [b] (Deshpande et al., 2001b); [c] (Dong et al., 2015); [d] (Dong and Wadley, 2015); [e] (Tankasala et al., 2015).
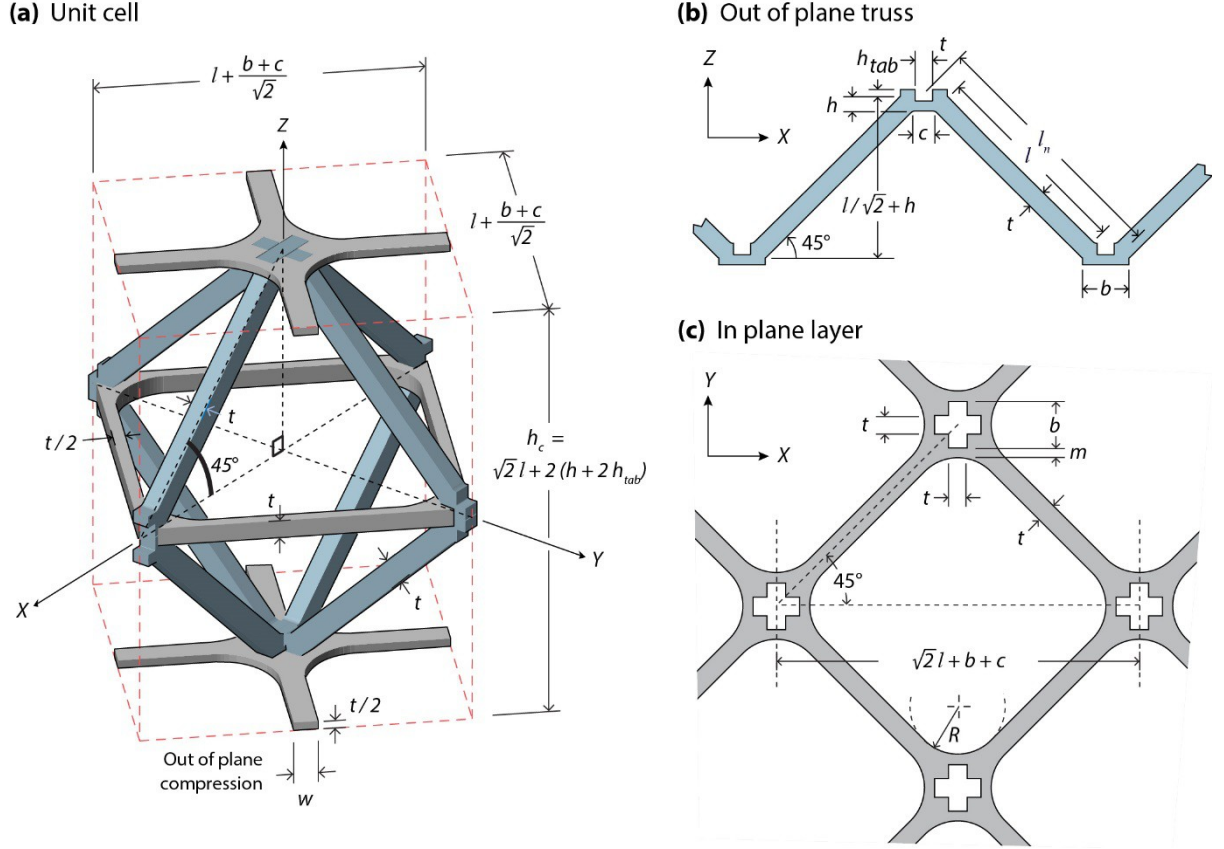
(a) Unit cell

(b) Out of plane truss

(c) In plane layer

Figure 3. Schematic illustrations of the presently studied snap-fit octet lattice unit cell (a), with its out-of-plane trusses (b) and *X-Y* layers (c).

For triangulated 2D lattices, finite element studies (Choi and Sankar, 2005; Fleck and Qiu, 2007; Huang and Gibson, 1991; Lipperman et al., 2007; Quintana-Alonso and Fleck, 2009; Tankasala et al., 2015) have shown the mode I fracture toughness, K_{Ic}, scales as:

$$K_{Ic} = \alpha \acute{\rho}^{d} \sigma_s \sqrt{l}$$

(1)

where the constants, α and d, are topology dependent. In general, the value of d is smaller for stretch dominated unit cells (for a triangular structure, $d = 1$) than for bending dominated unit cells (for a hexagonal structure, $d = 2$) (Tankasala et al., 2015) suggesting a significant benefit to using stretch dominated structures like the octet truss for low relative density structures. For foams (3D bending dominated structures), analytic and experimental studies have shown $d = 3/2$

(Gibson and Ashby, 1997). The fracture resistance of foams typically increases with crack length (i.e. rising R-curve behavior), where the stochasticity of a foam allows cell walls to survive behind the crack front and bridge the crack faces (McCullough et al., 1999; Olurin et al., 2000). Even so, their fracture toughness is very low, Fig. 1.

The 'snap-fit' method used by Dong et al. (Dong et al., 2015) offers a convenient method for making octet lattices for the study of fracture. In this method, layers of out of plane pyramidal trusses are combined with open face sheets of planar octet-truss, and the process repeated to create samples of arbitrary dimensions, Fig. 2b. The study reported here used thin Ti-6Al-4V alloy plates to fabricate the rows of out of plane trusses and the in plane truss layers, Fig. 3. This aerospace industry alloy has a strength to weight ratio almost twice that of aluminum alloys, a significantly higher maximum service temperature than aluminum or magnesium and excellent corrosion resistance (Donachie, 2000). The densities of the samples were varied by manipulating values for l and t (Table 2) and designed to fall between 300 and 850 kg m^{-3}. Mode I resistance curves are measured using a single edge notched bend (SENB) specimen design, and the toughness measured as a function of sample relative density and truss length. The results are then used to assess fracture toughness scaling as the cell size of a lattice decreases into the nanoscopic regime.

2. Sample design and fabrication

The unit cell of the octet-truss structure is shown in Fig. 3a. The trusses were square $t \times t$ in cross-section and oriented with an inclination angle of 45°. The free truss length between the nodes is given by l. The study examines six octet-truss structures arranged into two groups. One enabled variation of the relative density, $\bar{\rho}$ between 8 and 19%, with $l = 8$ mm fixed, while the

second enabled study of the effect of free truss length, l (varied between 4 and 15 mm), while $\acute{\rho}$ = 19% (fixed). The sample with l = 8 mm and $\acute{\rho}$ = 19% was common to both sets of samples, and is abbreviated as 19%-8 in Table 2.

Table 2. Sample dimensions. The measured relative density before and after addition of the braze alloy is denoted by $\acute{\rho}_a$ and $\acute{\rho}_b$, respectively. The remaining abbreviations are defined in Fig. 3 and 4.

	Sample	8%-8	11%-8	15%-8	19%-4	19%-8	19%-15
	$\bar{\rho}$ (%)	8.0	10.9	14.5	19.2	19.2	19.2
	l (mm)	7.5	7.5	7.5	3.8	7.5	15.1
	l_n (mm)	11.0	11.9	12.9	7.2	14.5	28.9
Nominal	t (mm)	1.0	1.3	1.6	1.0	2.0	4.1
	b (mm)	3.0	3.8	4.8	3.0	6.1	12.2
	c (mm)	1.4	1.8	2.2	1.4	2.9	5.7
	h (mm)	0.6	0.8	1.0	0.6	1.2	2.4
	h_{tab} (mm)	1.0	1.3	1.6	1.0	2.0	4.1
	m (mm)	0.9	1.1	1.3	0.8	1.7	3.3
	R (mm)	2.3	3.0	3.8	1.5	3.0	4.1
	$\bar{\rho_a}$ (%)	8.5	10.9	14.8	18.6	19.5	–
	$\bar{\rho_b}$ (%)	10.3	13.4	17.8	22.7	21.5	–
	l (mm)	7.5	7.8	8.2	4.1	7.9	17.5
Measured	l_n (mm)	11.2	12.1	13.4	7.4	14.5	30.0
	t (mm)	1.0	1.2	1.7	0.9	1.9	4.1
	B (mm)	31.3	33.9	37.0	20.7	41.3	82.3
	W (mm)	64	70	78	43	84	174
	S (mm)	260	280	310	170	340	697
	L (mm)	293	324	342	191	380	762

The relative density, $\acute{\rho}$, controls the l/t truss slenderness ratio, which is known to control both the compressive strength and the Young's modulus (Dong et al., 2015). The free truss length, l, is a proxy for the cell size. However, the actual separation distance between cells should be the appropriate length scaling for toughness. We therefore define the parameter l_n, the node-to-node truss length, Fig. 3b, as follows:

$$l_n = l \sqrt{\frac{(1+\acute{K}_3)^2 + (1+\acute{K}_4)^2}{2}} \qquad (2)$$

where $\acute{K}_3$ and $\acute{K}_4$ are defined in Table 1. The assembled structure is schematically shown in Fig. 4. It comprised nineteen unit cells repeated in the *X* direction and two unit cells repeated in the *Y* direction (with an extra ½ cell around the border to allow for complete nodal connections at the *X-Y* layers). Four unit cells were repeated in the *Z* direction (the outer two faces were of a full thickness *h*). Figure 4b identifies five *X-Z* planes, I-V, and nine *X-Y* layers denoted as 1-9 during discussion of the results. The width, *W*, thickness, *B*, and length, *L*, dimensions shown in Fig. 4 are given in Table 2. Figures 5a and b show photographs of the actual samples. X-ray computed tomographic (XCT) reconstructions of the samples are shown in Fig. 5c-f. The XCT reconstructions were used to calculate the relative density, $\acute{\rho}_b$ (the procedure is given in Appendix A). The relative density, $\acute{\rho}_a$, after removing the braze alloy mass was within a percentage point of the calculated nominal value, $\acute{\rho}$, given in Table 2. For simplicity, since the braze alloy had little effect on performance, we use the theoretical relative density value $\acute{\rho}$ in the remainder of the study.
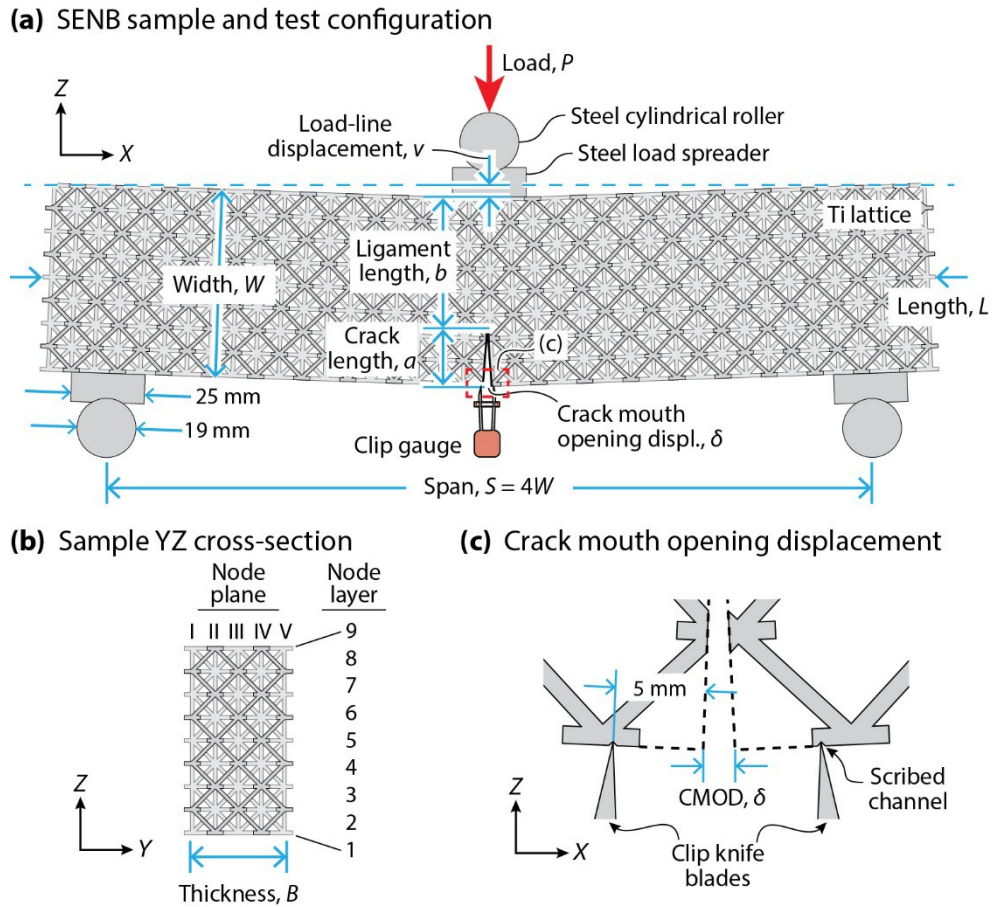
(a) SENB sample and test configuration

Load, *P*

Load-line displacement, *v*

Steel cylindrical roller

Steel load spreader

Z

X

Ti lattice

Ligament length, *b*

Width, *W*

Crack length, *a*

Length, *L*

(c)

25 mm

19 mm

Clip gauge

Crack mouth opening displ., *δ*

Span, *S* = 4*W*

(b) Sample YZ cross-section

Node plane

Node layer

I II III IV V

9
8
7
6
5
4
3
2
1

Z

Y

Thickness, *B*

(c) Crack mouth opening displacement

5 mm

Scribed channel

CMOD, *δ*

Z

X

Clip knife blades

Figure 4. (a) Side edge notched bend (SENB) sample and test configuration. (b) Side view of sample shown in (a). (c) Magnified inset from (a) showing measurement of the crack mouth opening displacement, *δ*.
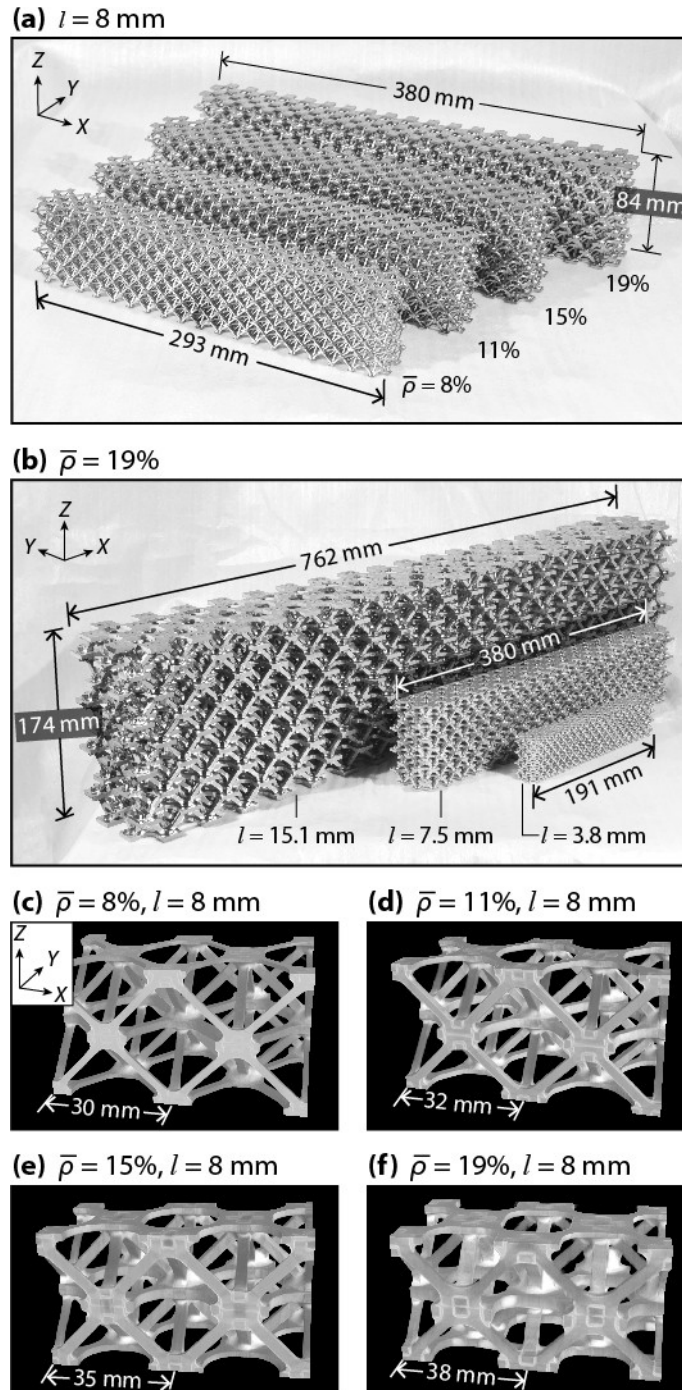
Figure 5. Photographs of Ti octet truss structures showing (a) four SENB samples with a truss length, l = 8 mm, and varying relative density, $\bar{\rho}$, and (b) three SENB samples with a relative density, $\bar{\rho}$ = 19%, and varying truss length, l. (c-e) XCT reconstructions of l = 8 mm samples.

Fabrication of the structures followed the procedures given in Ref. (Dong et al., 2015). The structures were assembled by 'snap-fitting' together pieces having one of two geometries, Fig. 3b and c. The pieces were water-jet cut from h thick plates of the titanium alloy Ti-6Al-4V to the dimensions given in Table 2. The Ti-6Al-4V alloy had a measured Young's modulus, $E_s = 123$ GPa, and tensile yield strength, $\sigma_s = 930$ MPa (Dong et al., 2015). Prior to assembly, the nodes were coated with a 40Ti-20Cu-20Ni-20Zr (wt.%) braze alloy (Lucas Milhaupt, WI, USA). Each assembled structure was then vacuum brazed for 30 min. at a chamber pressure of ~5x10^{-2} Pa and a temperature of 900°C. This temperature was above the 848°C solidus temperature of the braze alloy but below the 980°C solidus temperature of the β-phase of the Ti-6V-4Al alloy. This allowed the Ti-6V-4Al alloy to maintain its equiaxed α-grain and intergranular β-phase, while the braze alloy could flow to fill the gaps at the nodes, Fig. 6b. A ~100 μm thick diffusion zone was formed between the braze and Ti-6V-4Al alloy, and contained regions with a fine Widmanstätten structure and a β-Ti rich region. Each sample was annealed at 600°C for 20 min. to reduce internal residual stress before finally cooling to ambient temperature.

After brazing, a notch was cut through three *X-Y* layers, Fig. 4a, using wire electrical discharge machining (EDM). The wire was aligned along the *Y* sample direction and grazed a side of the *Y-Z* oriented trusses at the sample mid-span.
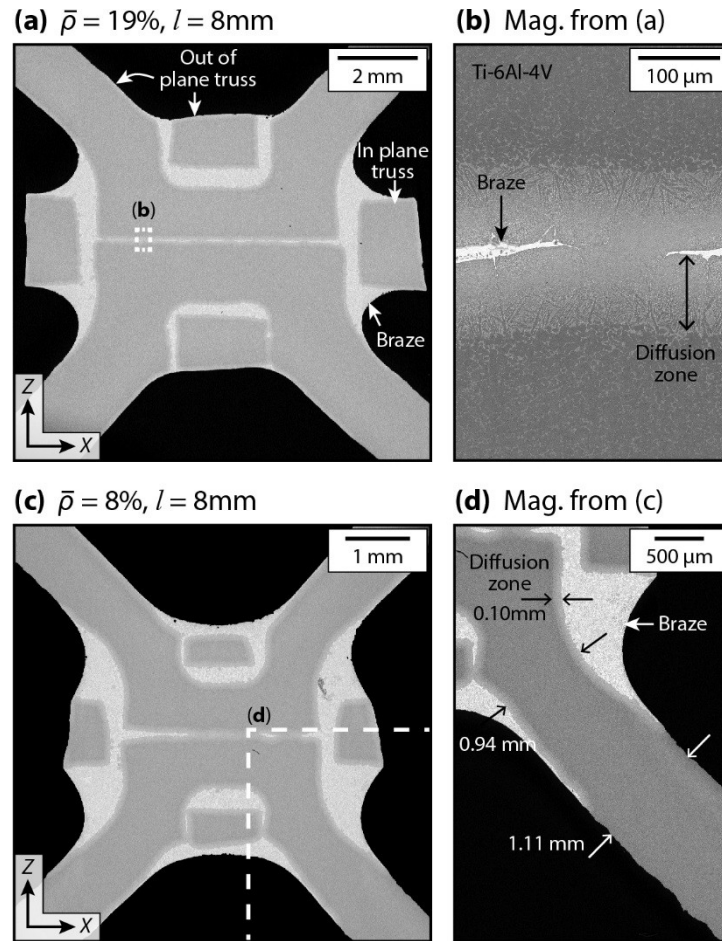
Figure 6. SEM micrograph of an *X-Z* cross-section through the node of (a) an 8%-8 and (c) a 19%-8 sample. (b) Magnification of the brazed joint identified in (a). (d) Magnification of the truss identified in (c).

3. Fracture toughness measurement methodology

The fracture resistance was determined in mode I using a singled edge notch bend (SENB) sample. A single sample of each combination of relative density, $\bar{\rho}$, and free truss length, *l*, was tested in three point bending, Fig. 4a. The two outer steel rollers defined the span, *S*, which was adjusted to be about four times the sample width, *W*. The third roller was located at the mid-span, opposite the sample notch. Steel load spreaders placed between the rollers and the sample

prevented local indentation. The tests were performed with an Instron (Buckinghamshire, UK), model 5500R, universal testing machine at a constant crosshead displacement rate. To maintain a fixed nominal strain rate for the different span samples, the displacement rate was set at 0.05, 0.1 or 0.2 mm min^{-1} for samples with l = 4, 8 or 15 mm, respectively, Table 2. A laser extensometer, model LE-05 (Electronic Instrument Research, PA, USA) measured the load-line displacement, v, and an Instron clip-gauge (Cat. No. 2620-602 or 2620-604), measured the crack mouth opening displacement, δ. Each knife-edge of the clip gauge rested in a groove scribed into the bottom of the sample on either side of the notch, Fig. 4c.

The *J*-integral approach was employed to capture inelastic contributions to the fracture resistance using the elastic compliance method in Ref. (ASTM E182, 2013). Compliance measurements from the unloading curves were made at intervals Δv = 0.1, 0.2 and 0.4 mm for the l = 4, 8 or 15 mm samples, respectively. Calculation of the current crack length used the compliance along the loading line, and the *J*-integral was calculated using the measured applied load and crack mouth opening displacement, δ. The stress intensity factor, K_J, is related to the *J*-integral by $K_J = \sqrt{E' J}$, where E' is traditionally the plain strain Young's modulus, $E' = E_s/(1 - v^2)$ and v is Poisson's ratio. Since the samples were lattices and not homogeneous solid materials, this study used the measured compressive moduli along the span length, Fig. B1. The experimental details are provided in Appendix B, and the modulus and strength values of each sample are tabulated in Table 3. Appendix C provides additional details on calculating the fracture toughness.

Table 3. The measured in-plane Young's modulus, E_{XX}, in-plane compressive 0.2% offset yield stress, σ_{XX}^{y}, peak strength, σ_{XX}^{p}, and fracture toughness, K_{JIc}.

Sample	8%-8	11%-8	15%-8	19%-4	19%-8	19%-15
E_{XX} (GPa)	2.0	2.8	4.4	6.2	5.9	6.4
σ_{XX}^{y} (MPa)	20	32	46	61	57	59
σ_{XX}^{p} (MPa)	21	32	49	68	67	69
K_{JIc} (MPa m$^{1/2}$)	2.5	4.6	7.3	7.2	9.6	13.8

4. Fracture toughness measurements

Figure 7 plots the load, *P,* as a function of both load-line displacement, *v*, and crack mouth opening displacement, *δ*, for the 19%-8 sample. The load increased with *v* until reaching a pair of peaks at P ≈ 15 kN and *v* ≈ 3 mm. In-situ images of the node immediately ahead of the wire EDM notch are shown in Fig. 8 (a video is available as online supplementary information). Before the peak load, a pair of *X-Y* planar failures through the node are visible above and below Layer 4 (see Fig. 4b for planar references), as well as failure at a node-truss interface, Fig. 8c. After peak load, the remaining node-truss interfaces failed, and a *Z* shaped crack split the node, Fig. 8d. The drop in load after this pair of peaks has been labeled with an encircled number one in Fig. 7 and demarks the failure of Layer 4 ahead of the notch as shown in Fig. 9a. With further loading, the subsequent layer (Layer 5) failed by a similar sequence, followed by Layer 6, Fig. 7 and 9a.
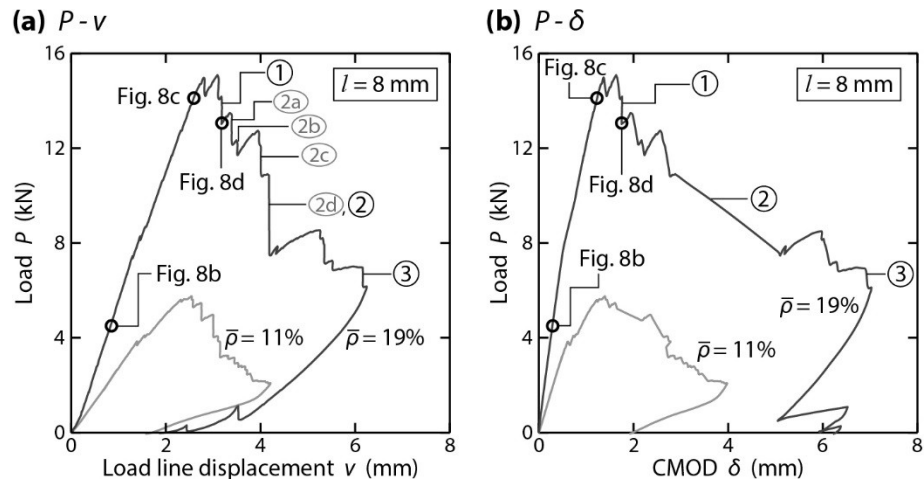
Figure 7. Representative responses of SENB samples showing the load, *P*, as a function of (a) the load line displacement, *v*, and (b) the crack mouth opening displacement, *δ*. Unload-reload compliance measurements have been removed for clarity.
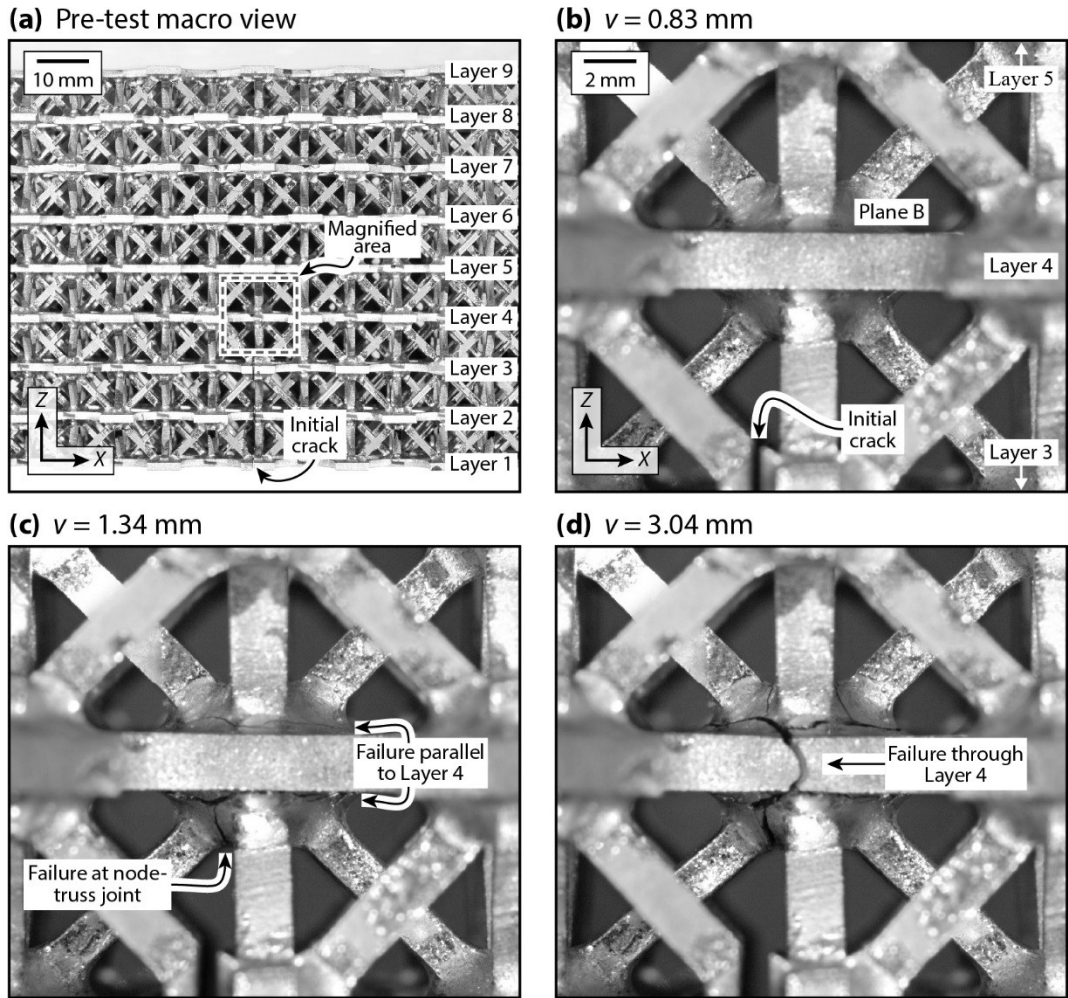
Figure 8. (a) The node immediately ahead of the initial notch within a 19%-8 SENB sample. (b-d) In-situ photographic sequence of the identified node in (a). The displacement of each image is identified in Fig. 7b.
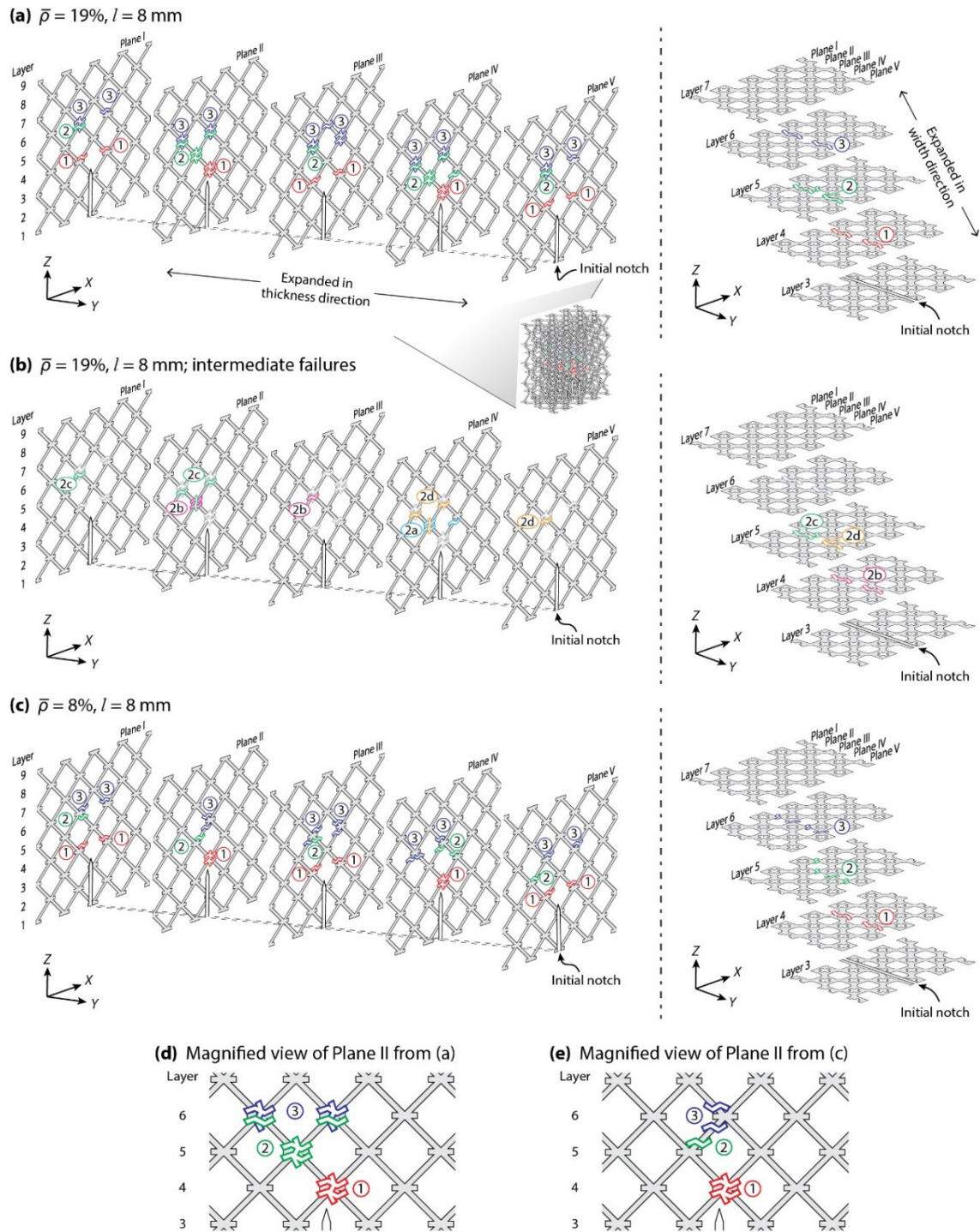
Figure 9. Schematic illustration of the failure sequence of a 19%-8 (a-b) and an 8%-8 (c) SENB sample. Magnified views of parts (a) and (c) and shown in (d) and (e), respectively. Layers 1-9 and Planes I-V have been separated for clarity. The encircled numbers show the observed failure locations at the points identified in Fig. 7.

The general failure characteristics for this structure are as follows: Damage was predominately isolated to the layer ahead of the crack front. Initially, micro-cracks formed above and below the node within the braze, as well as node-truss interface failures, with the failure location interchanging between all five (I-V) planes, Fig. 9b. Finally, the crack advanced through the nodes. The layer-by-layer advancement of the crack precluded toughening by crack bridging, as is commonly observed with foams. However, the damage accumulated at the nodes and the variability of in-plane failure location both could contribute to crack tip shielding mechanisms.

For the smallest relative density sample (8%-8), failure switched from the nodes, Fig. 10a, to failure of the individual trusses, Fig. 10b. A schematic of the failure locations is shown in Fig. 9c for comparison against Fig. 9a (also see insets shown in Fig. 9d and e). The intermediate relative density samples failed in a mixed manner, transitioning from predominately truss failure to nodal failure with increasing $\acute{\rho}$. Similarly, the smallest cell size sample predominately exhibited truss failure; consistent with truss failure being the dominant mode for thinner truss samples.
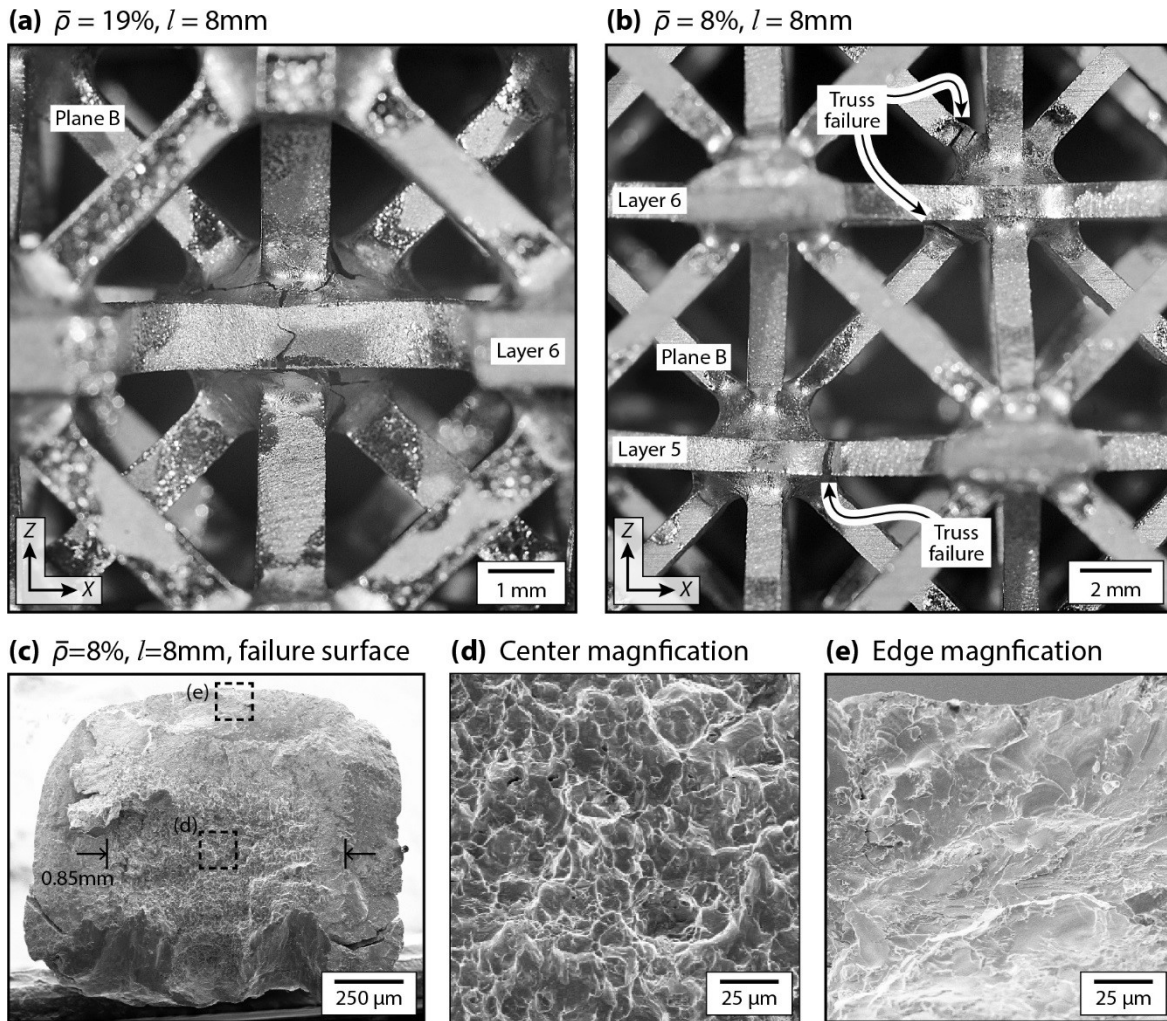
Figure 10. Post-mortem image of (a) the 8%-8 sample showing truss failure and (b) the 19%-8 sample showing node failure. (c) Truss failure surface from the 8%-8 sample, with magnifications near (d) the center and (e) the edge.

Micrographs through the nodes of samples 19%-8 and 8%-8 are shown in Fig. 6. Where the truss meets the node, a fabrication constraint lead to a reduction of the truss thickness from 1.1 mm to 0.9 mm, as highlighted in Fig. 6d. This issue was less evident with thicker truss samples, Fig. 6a. The location of truss failure identified in Fig. 10b is consistent with that of the truss thinning near the node. A micrograph of a truss failure surface recovered from the 8%-8

sample reveals dimpling typical of ductile microvoid coalescence in the center 0.8 mm × 0.8 mm region, and brittle failure of the braze near the edges, Fig. 10c-e.

The fracture toughness, K_J, calculated using the J-integral, is plotted against crack extension, Δa, in Fig. 11. The fracture resistance clearly depended upon relative density and cell size. It remained nearly constant with crack extension for the 8%-8 sample, while approximately doubling after the crack extended $\Delta a = 1.5l_n$ for the 19%-15 sample (R-curve effect). In general, the relative increase in fracture resistance with crack growth was greater for samples with larger $\acute{\rho}$ and l. Recall from Fig. 9 that the fracture mode (and location) changed from truss dominated to node dominated as both $\acute{\rho}$ and l increased. The plastic deformation at the nodes causes dissipation which results in a moderate rise in fracture resistance with Δa. This becomes more pronounced with increases in nodal volume; hence, the R-curve effect increased with increases in $\acute{\rho}$ and l.
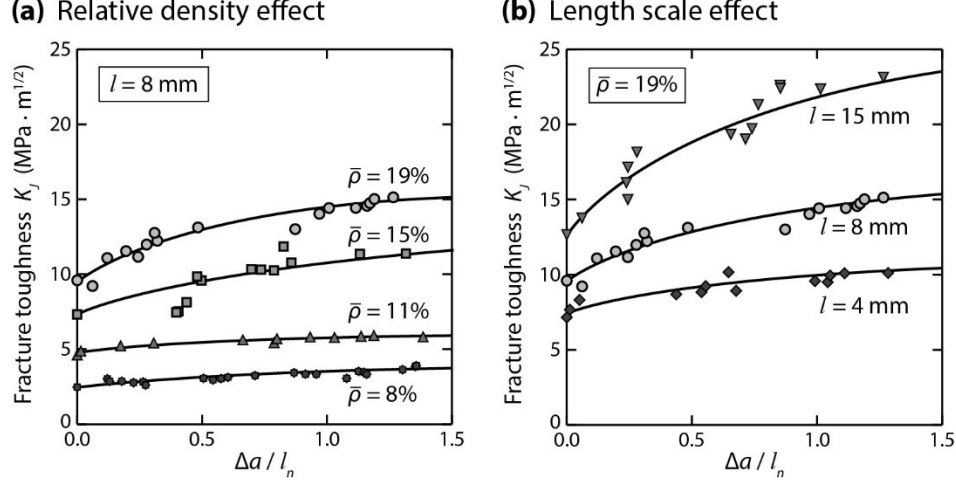
Figure 11. SENB fracture toughness, K_J, response as a function of the crack length, Δa, normalized by the node-to-node truss length, l_n, for (a) $l = 8$ mm samples having different relative densities, $\bar{\rho}$, and (b) $\bar{\rho} = 19\%$ samples having different truss lengths, l. Lines through the data were added to aid the reader.

Figure 12 summarizes the mode I toughness at zero crack extension, K_{JIc}: the toughness K_{JIC} increased with both relative density and cell size (the values are given in Table 3). Figure 13 replots these two dependencies after normalizing K_{JIc} such that the slope of a line fitting the data, and passing through origin, gives the dimensionless variable α from Eq. 1, assuming $d = 1$. Note that Fig. 12 and 13 use the length l_n, which measures the node-to-node spacing. From the fit to the data, we see the fracture toughness of the snap fit octet lattice is given by:

$$K_{Ic} = 0.45\, \acute{\rho}\, \sigma_s \sqrt{\acute{l}} \sqrt{\frac{\left(1+\acute{K}_3\right)^2 + \left(1+\acute{K}_4\right)^2}{2}} \tag{3}$$

and confirms the linear dependency on $\acute{\rho}$ (i.e. $d = 1$). This dependence is less aggressive than the $\geq 3/2$ power dependency commonly observed with foams and other bending dominated structures, which rapidly loose toughness with decreasing $\acute{\rho}$ (Choi and Sankar, 2005; Tankasala

23

et al., 2015). The value of $\alpha = 0.45$ for the octet lattice is similar to the 2D triangular lattice, Table 1: this is notable as the octet lattice is formulated from a triangular lattice but now with an arrangement of nodes in 3-dimensional space.
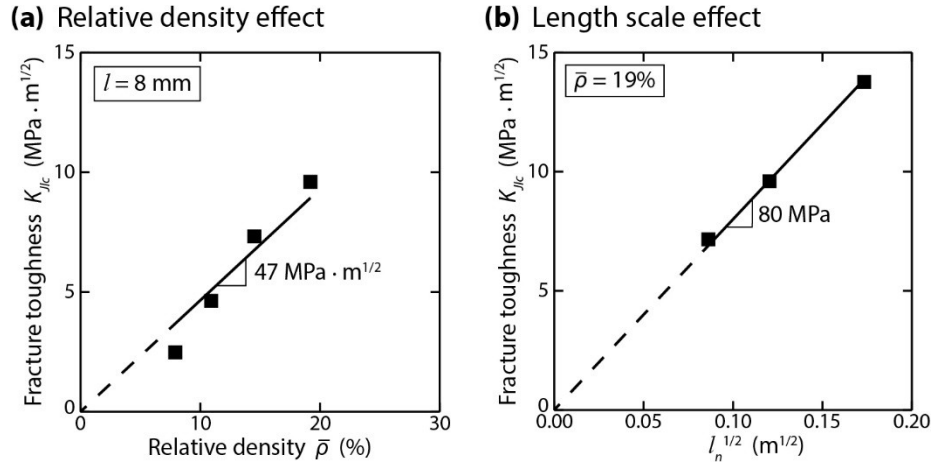

Figure 12. The effect of (a) the relative density, $\bar{\rho}$, and (b) the cell size (given by the node-to-node truss length, l_n) on the fracture toughness, K_{JIc}.
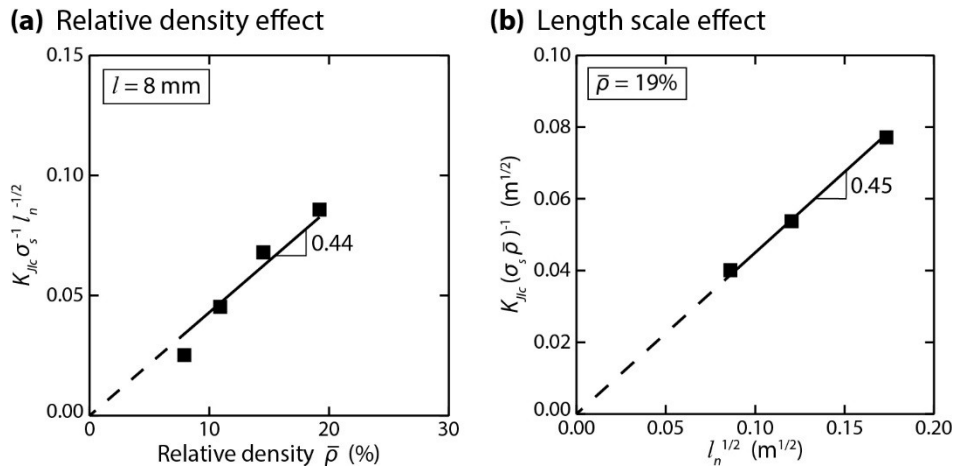

Figure 13. The effect of the relative density, $\bar{\rho}$, (a) and the node-to-node truss length, l_n, (b) on the normalized fracture toughness.

5. Discussion

The measured fracture toughness and compressive yield strength, σ_{XX}^{y}, (see Appendix B for details) values for the Ti octet truss structure are compared with other materials in Fig. 1. Compared to materials of similar density (300 to 1000 kg m^{-3}), the titanium octet truss studied here had the highest combination of strength and toughness. The next highest ranked material was wood, but this is an anisotropic material, and only competes with the octet lattice in its highest performing direction (when cracks are propagated transversely to the grain direction).

It is interesting to note that methods capable of fabricating microlattices with nanoscale features are emerging (Meza et al., 2014; Zheng et al., 2014), and since the toughness scales with truss length, experimental validation permits comment on their likely fracture toughness. When a single crystal metallic truss measures approach micron thicknesses, the yield strength is no longer invariant of the truss size, and instead will increase with decreasing thickness (Greer and De Hosson, 2011). While the mechanisms controlling this behavior are still a subject of debate, one proposed mechanism, dislocation starvation, argues dislocations annihilate at the sample free surface, depleting the crystal of dislocations and increasing the yield strength (Greer et al., 2005; Greer and Nix, 2006; Greer and De Hosson, 2011). For single crystal face-centered cubic (FCC) metals, a simple power-law model empirically captures the size effect. Dou and Derby (Dou and Derby, 2009) proposed that for gold, copper and nickel data, the critical resolved shear strength τ_{s} for the {1 1 1}<1 1 0> slip system scaled by the shear modulus μ, is well approximated by a relation of the form:

$$\tau_s = \begin{cases} 0.71\,\mu\,(t/b)^{-0.66}, \wedge t < t_c \\ \sigma_b/2, \wedge t \geq t_c \end{cases} \qquad (4)$$

where b is the Burgers vector and t is the truss thickness, while σ_b is the bulk, size-independent tensile yield strength of the material and t_c is the smallest truss thickness for size-independent behavior which is given by $t_c = b\left(\dfrac{1.42\,\mu}{\sigma_b}\right)^{1.51}$. Using Eq. 4 and the values of μ, b and σ_b provided in Table 4, the predicted yield strength ($\sigma_s = 2\tau_s$) as a function of truss thickness for each of these metals is shown in Fig. 14a. Figure 14b shows the predicted fracture toughness of an octet truss lattice comprised of these metals. Once the truss enters a strength-size dependent regime, Eq. 3 predicts that the strengthening leads to an increase in fracture toughness with decreasing cell size. This is a reversal of the macroscopic behavior as the reduction in toughness, due to decreasing cell size, is more than offset by the increase in yield strength. Thus, there is a potentially significant benefit to the toughness of nano-scale lattices if methods can be developed to make them.

Table 4. The resolved shear modulus, μ, the Burgers vector, b, and the bulk, size-independent strength, σ_b, is provided for three FCC metals.

Material	μ (GPa) [a]	b (nm) [b]	σ_b (MPa) [b]
Gold	18.7	0.288	60
Copper	30.5	0.256	150
Nickel	59.3	0.250	70

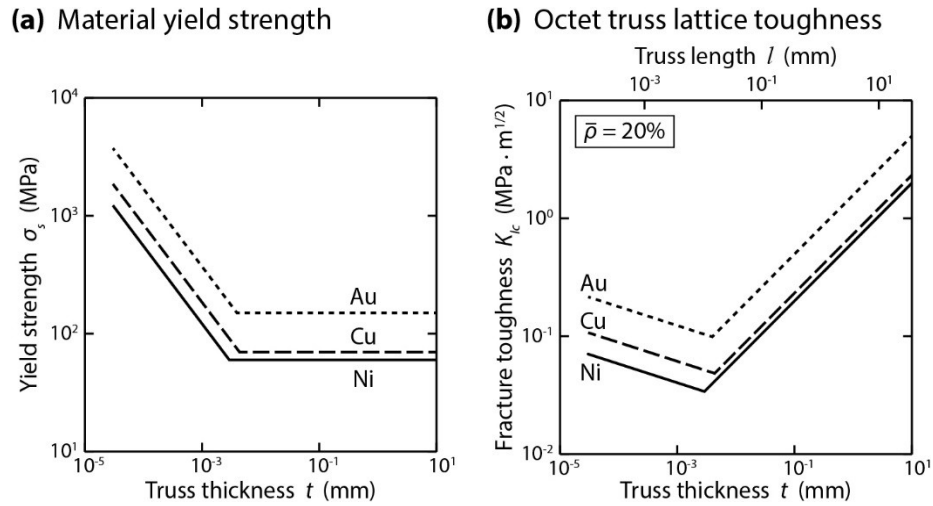References: [a] (Dou and Derby, 2009); and [b] (*CES EduPack*, 2015).

Figure. 14. (a) Predicted material yield strength dependence on truss thickness for single crystal gold, copper and nickel trusses, using Eq. 4. (b) Predicted fracture toughness of an octet truss using Eq. 3 and the predictions shown in part (a).

6. Final remarks

An experimental study of the mode I fracture resistance of the octet truss structure has been conducted. A scalable 'snap-fit' fabrication procedure was used to assemble Ti-6Al-4V lattice structures with relative densities of 8 to 19%, and with cell sizes (truss lengths) of 4 to 15 mm. Single edge notched bend (SENB) samples were tested in three-point bending at a constant rate of displacement, and the *J*-integral method was employed to calculate their fracture resistance. The fracture toughness of the structure was shown to increase linearly with both the relative density and the square root of the cell size. The measured toughness values were in the range of 2 to 14 MPa m$^{1/2}$. The crack advanced cell by cell through the structure, with numerous micro failure events within each cell layer prior to fracturing. A moderate increase in fracture resistance

with crack growth was seen for larger relative density and cell size samples. It was proposed these geometries benefit from plastic deformation within the larger nodal volumes.

With elastic moduli and compressive strengths in the range of 2 to 6 GPa and 20 to 70 MPa, respectively, the titanium snap-fit octet truss structures studied are a more isotropic and lighter material solution to engineering designs than woods, and may be utilized at substantially higher service temperatures than natural or polymeric material alternatives.

Acknowledgements

Appendix A. Relative density measurement

Relative density measurements were made from X-ray computed tomographic (XCT) reconstructions. A volume containing 4×2×4 unit cells in the X, Y and Z directions, respectively was scanned (XTEC model XT H 225 ST, Nikon Metrology UK). The sensitivity of the X-rays to material density allowed the air, Ti-6V-4Al alloy and braze alloy to be distinguished, Fig. A1a and c. Higher density materials are rendered brighter, with air and braze defined as two extremities of black and white, respectively. The relative density without the braze, $\acute{\rho}_a$, was measured from 2×2×2 unit cell volumes by calculating the volume solely occupied by the Ti alloy, using the mask shown in Fig. A1b and d. The measurement $\acute{\rho}_b$ gives the relative density including the braze. The measurement range from multiple samplings and from changing the

28

masking settings gave a confidence interval of ±5% of the results provided in Table 2. The signal

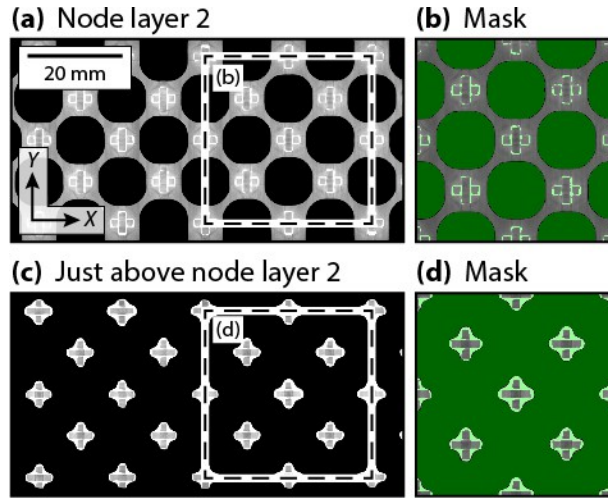attenuation from the largest sample, 19%-15, was too great to allow for quantitative analysis.

Figure A1. XCT reconstruction of the 15%-8 sample showing an *XY* cross-section through (a) node layer 2 and (c) a section adjacent to node layer 2. (b) and (d) mask the air and braze portions of the insets shown in (a) and (c).

Appendix B. In-plane compression

The in-plane modulus, E_{XX}, was measured in compression, Fig. B1a. Each sample type was one unit cell tall in the *X* direction and had the same thickness, *B*, and width, *W*, as in the fracture toughness test (dimensions are given Table 2). The samples were compressed at a constant cross-head displacement rate, which was set for an initial strain rate of 10^{-4} s^{-1}. The nominal stress, σ_{XX}, was calculated using the initial loading area $B \times W$, and the nominal strain, ε_{XX}, was calculated from the displacement normalized by the unit cell height, h_c.
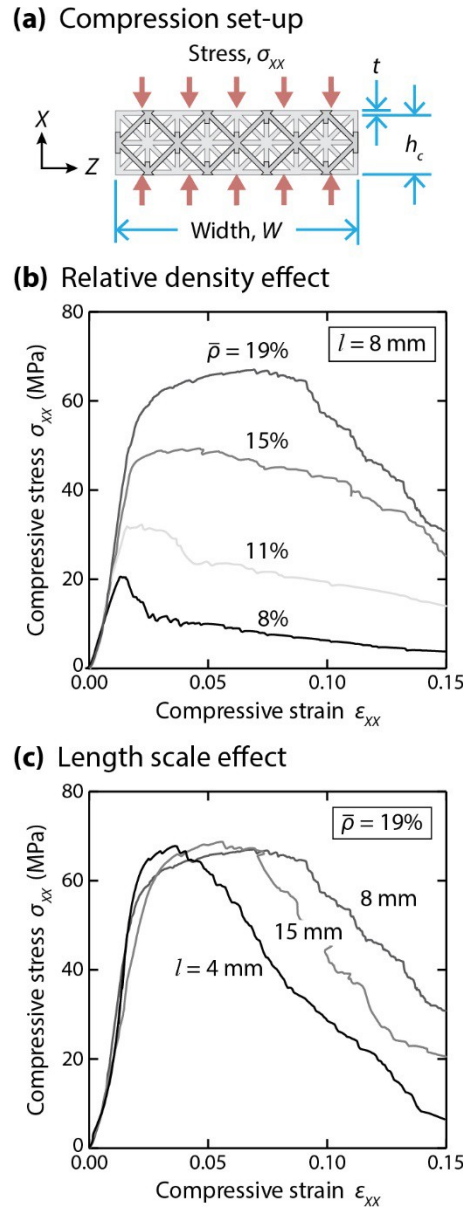
Figure B1. (a) The in-plane compression test configuration. The compressive stress-strain response for (b) l = 8 mm samples with different relative densities, $\bar{\rho}$, and (c) $\bar{\rho}$ = 19% samples with different truss lengths, l.

The stress-strain responses are provided in Fig. B1b and c to illustrate both the effect of relative density and cell size. Expectedly, there is an elastic regime prior to reaching a peak stress which is then followed by a softening regime (a full analysis of the compressive behavior is given in Ref. (Dong et al., 2015)). The modulus was measured from unloading curves performed

in the elastic regime. Figure B2 plots the measured modulus, E_{XX}, and peak strength, σ_{XX}^{p}, values

as a function of relative density, with the values provided in Table 3. Figure B2 also shows the

values predicted when using the relationships provided in Table 1 with both the modulus and

strength given by the analytical formula in Table 1 increased by a factor of 1.1875 to account for

the additional trusses along the sample border as compared to the unit cell ideal. The

measurements are in good agreement with predictions, with a moderate under-prediction of the

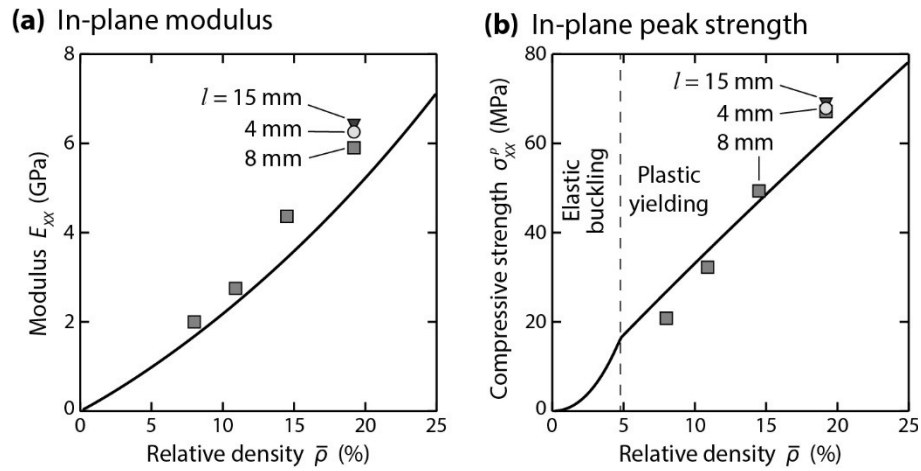modulus as the compliance from bending of the struts was neglected in the analysis.

Figure B2. In-plane Young's modulus, E_{XX}, (a) and compressive peak strength, σ_{XX}^{p}, (b) as

functions of the relative density, $\bar{\rho}$. Solid lines are sample predictions using the relations in Table

1.

Appendix C. Fracture toughness calculations

Calculation of the fracture toughness followed the procedure outlined in Annex A1 from

Ref. (ASTM E182, 2013). We summarize it below for completeness. The J-integral is taken to be

comprised of an elastic component, J_{el}, and a plastic component, J_{pl}. The two components are

calculated at the onset of every unloading cycle (given by the index *i*) performed in the loading regime. The value of *J* at instant *(i)* in the loading regime is then given by the summation

$$J_{(i)} = J_{el(i)} + J_{pl(i)} \tag{C.1}$$

The elastic component $J_{el(i)}$ follows from

$$J_{el(i)} = K_{(i)}^2 / E_{XX} \tag{C.2}$$

where the typical plane strain modulus E' has been replaced with the measured value E_{XX}. The value of $K_{(i)}$ at each unload event is given as

$$K_{(i)} = \frac{P_i S}{B W^{3/2}} f(a_i/W) \tag{C.3}$$

where P_i is the value of the load at the onset of unloading. The geometrical parameters *S*, *B*, and *W* are defined in Fig. 4, and the calibration factor $f(a_i/W)$ is given by

$$f(a_i/W) = 3\left(\frac{a_i}{W}\right)^{1/2} \frac{\left[1.99 - \left(\frac{a_i}{W}\right)\left(1 - \frac{a_i}{W}\right)\left(2.15 - 3.93\frac{a_i}{W} + 2.7\left(\frac{a_i}{W}\right)^2\right)\right]}{2\left(1 + 2\frac{a_i}{W}\right)\left(1 - \frac{a_i}{W}\right)^{3/2}} \tag{C.4}$$

where $a_{(i)}$ is the current crack length. This crack length is estimated using the relation

$$a_{(i)} = W\left(0.999748 - 3.9504\,u + 2.9821\,u^2 - 3.21408\,u^3 + 51.51564\,u^4 - 113.031\,u^5\right) \tag{C.5}$$

where the factor *u* is related to the compliance via

$$u = \left[\left(4BW\,E_{XX}\,C_{\delta(i)}/S\right)^{1/2} + 1\right]^{-1} \tag{C.6}$$

where $C_{\delta(i)} \equiv \left(\dfrac{dP}{d\delta}\right)_{(i)}$ is the compliance estimated from the crack mouth opening displacement at

the onset of unloading.

The plastic component of J is estimated using the deformation J definition via

$$J_{pl(i)} = \left[J_{pl(i-1)} + \left(\frac{\eta_{pl}}{b_{(i-1)}}\right)\left(\frac{A_{pl(i)} - A_{pl(i-1)}}{B}\right) \right]\left[1 - \gamma_{pl}\left(\frac{a_{(i)} - a_{(i-1)}}{b_{(i-1)}}\right) \right] \quad (C.7)$$

where $\eta_{pl} = 1.9$, $\gamma_{pl} = 0.9$, b is the length of the uncracked ligament (see Fig. 4a) at the previous

unloading event, and $A_{pl(i)}$ is the area under the plastic load versus load-line displacement

measurement. We estimate $A_{pl(i)}$ using

$$A_{pl(i)} = A_{pl(i-1)} + \left(P_{(i)} + P_{(i-1)}\right)\left(v_{pl(i)} - v_{pl(i-1)}\right)/2 \quad (C.8)$$

where $v_{pl(i)} = v_{(i)} - P_{(i)}C_{v(i)}$ is the plastic part of the load-line displacement measurement and

$C_{v(i)} \equiv \left(\dfrac{dP}{dv}\right)_{(i)}$ is the compliance estimated from the load-line displacement.

The fracture toughness at the unloading instant *(i)*, $K_{J(i)}$, is then calculated from the *J*-

integral using the usual relation $K_{J(i)} = \left(J_{(i)} E_{XX}\right)^{1/2}$.

References

Ashby, M., 2011. Hybrid Materials to Expand the Boundaries of Material-Property Space. J. Am. Ceram. Soc. 94, s3–s14. doi:10.1111/j.1551-2916.2011.04559.x

ASTM E182, 2013. Standard Test Method for Measurement of Fracture Toughness. ASTM International, West Conshohocken, PA. doi:10.1520/E1820-13E01

Bauer, J., Hengsbach, S., Tesari, I., Schwaiger, R., Kraft, O., 2014. High-strength cellular ceramic composites with 3D microarchitecture. PNAS 111, 2453–2458. doi:10.1073/pnas.1315147111

Bauer, J., Schroer, A., Schwaiger, R., Kraft, O., 2016. Approaching theoretical strength in glassy carbon nanolattices. Nat Mater advance online publication. doi:10.1038/nmat4561

CES EduPack, 2015. . Granta Design Limited.

Cheung, K.C., Gershenfeld, N., 2013. Reversibly Assembled Cellular Composite Materials. Science 341, 1219–1221. doi:10.1126/science.1240889

Choi, S., Sankar, B.V., 2005. A micromechanical method to predict the fracture toughness of cellular materials. International Journal of Solids and Structures 42, 1797–1817. doi:10.1016/j.ijsolstr.2004.08.021

Deshpande, V.S., Ashby, M.F., Fleck, N.A., 2001a. Foam topology: bending versus stretching dominated architectures. Acta Materialia 49, 1035–1040. doi:10.1016/S1359-6454(00)00379-7

Deshpande, V.S., Fleck, N.A., Ashby, M.F., 2001b. Effective properties of the octet-truss lattice material. Journal of the Mechanics and Physics of Solids 49, 1747–1769. doi:10.1016/S0022-5096(01)00010-2

Donachie, M.J., 2000. Titanium: A Technical Guide, 2nd ed. ASM International, Materials Park, OH.

Dong, L., Deshpande, V., Wadley, H., 2015. Mechanical response of Ti–6Al–4V octet-truss lattice structures. International Journal of Solids and Structures 60–61, 107–124. doi:10.1016/j.ijsolstr.2015.02.020

Dong, L., Wadley, H., 2015. Mechanical properties of carbon fiber composite octet-truss lattice structures. Composites Science and Technology 119, 26–33. doi:10.1016/j.compscitech.2015.09.022

Dou, R., Derby, B., 2009. A universal scaling law for the strength of metal micropillars and nanowires. Scripta Materialia 61, 524–527. doi:10.1016/j.scriptamat.2009.05.012

Finnegan, K., Kooistra, G., Wadley, H.N.G., Deshpande, V.S., 2007. The compressive response of carbon fiber composite pyramidal truss sandwich cores. IJMR 98, 1264–1272. doi:10.3139/146.101594

Fleck, N.A., Qiu, X., 2007. The damage tolerance of elastic–brittle, two-dimensional isotropic lattices. Journal of the Mechanics and Physics of Solids 55, 562–588. doi:10.1016/j.jmps.2006.08.004

Gibson, L.J., Ashby, M.F., 1997. Cellular Solids: Structure and Properties. Cambridge University Press.

Greer, J.R., 2015. Materials by design: Using architecture and nanomaterial size effects to attain unexplored properties. Bridge 45, 37–44.

Greer, J.R., De Hosson, J.T.M., 2011. Plasticity in small-sized metallic systems: Intrinsic versus extrinsic size effect. Progress in Materials Science, Festschrift Vaclav Vitek 56, 654–724. doi:10.1016/j.pmatsci.2011.01.005

Greer, J.R., Nix, W.D., 2006. Nanoscale gold pillars strengthened through dislocation starvation. Phys. Rev. B 73, 245410. doi:10.1103/PhysRevB.73.245410

Greer, J.R., Oliver, W.C., Nix, W.D., 2005. Size dependence of mechanical properties of gold at the micron scale in the absence of strain gradients. Acta Materialia 53, 1821–1830. doi:10.1016/j.actamat.2004.12.031

Huang, J.S., Gibson, L.J., 1991. Fracture toughness of brittle foams. Acta Metallurgica et Materialia 39, 1627–1636. doi:10.1016/0956-7151(91)90250-5

Jang, D., Meza, L.R., Greer, F., Greer, J.R., 2013. Fabrication and deformation of three-dimensional hollow ceramic nanostructures. Nat Mater 12, 893–898. doi:10.1038/nmat3738

Kooistra, G.W., Deshpande, V.S., Wadley, H.N.G., 2004. Compressive behavior of age hardenable tetrahedral lattice truss structures made from aluminium. Acta Materialia 52, 4229–4237. doi:10.1016/j.actamat.2004.05.039

Lipperman, F., Ryvkin, M., Fuchs, M.B., 2007. Fracture toughness of two-dimensional cellular material with periodic microstructure. Int J Fract 146, 279–290. doi:10.1007/s10704-007-9171-5

McCullough, K.Y.G., Fleck, N.A., Ashby, M.F., 1999. Toughness of aluminium alloy foams. Acta Materialia 47, 2331–2343. doi:10.1016/S1359-6454(99)00125-1

Meza, L.R., Das, S., Greer, J.R., 2014. Strong, lightweight, and recoverable three-dimensional ceramic nanolattices. Science 345, 1322–1326. doi:10.1126/science.1255908

Montemayor, L., Chernow, V., Greer, J.R., 2015. Materials by design: Using architecture in material design to reach new property spaces. MRS Bulletin 40, 1122–1129. doi:10.1557/mrs.2015.263

Olurin, O.B., Fleck, N.A., Ashby, M.F., 2000. Deformation and fracture of aluminium foams. Materials Science and Engineering: A 291, 136–146. doi:10.1016/S0921-5093(00)00954-0

Quintana-Alonso, I., Fleck, N.A., 2009. Fracture of Brittle Lattice Materials: A Review, in: Daniel, I.M., Gdoutos, E.E., Rajapakse, Y.D.S. (Eds.), Major Accomplishments in Composite Materials and Sandwich Structures. Springer Netherlands, pp. 799–816.

Tankasala, H.C., Deshpande, V.S., Fleck, N.A., 2015. 2013 Koiter Medal Paper: Crack-Tip Fields and Toughness of Two-Dimensional Elastoplastic Lattices. J. Appl. Mech 82, 091004–091004. doi:10.1115/1.4030666

Torrents, A., Schaedler, T.A., Jacobsen, A.J., Carter, W.B., Valdevit, L., 2012. Characterization of nickel-based microlattice materials with structural hierarchy from the nanometer to the millimeter scale. Acta Materialia 60, 3511–3523. doi:10.1016/j.actamat.2012.03.007

Wadley, H.N.G., 2006. Multifunctional periodic cellular metals. Philosophical Transactions of the Royal Society A 31–68.

Zheng, X., Lee, H., Weisgraber, T.H., Shusteff, M., DeOtte, J., Duoss, E.B., Kuntz, J.D., Biener, M.M., Ge, Q., Jackson, J.A., Kucheyev, S.O., Fang, N.X., Spadaccini, C.M., 2014. Ultralight, ultrastiff mechanical metamaterials. Science 344, 1373–1377. doi:10.1126/science.1252291